Tuning transport properties via rare-earth doping and epitaxial strain in Sr_2IrO_4 thin films

Jiangfeng Yang [1,2] Wei Guo,[1,2] Zhihang Xu,[3] Yuwei Liu,[1,2] Haoying Sun [1,2] Wenjie Sun [1,2] Shengjun Yan,[1,2] Yueying Li [1,2] Zhengbin Gu [1,2] Jian Zhou [1,2] Ye Zhu [3,*] and Yuefeng Nie [1,2,†]

[1]*National Laboratory of Solid State Microstructures, Jiangsu Key Laboratory of Artificial Functional Materials, College of Engineering and Applied Sciences, Nanjing University, Nanjing 210093, China*

[2]*Collaborative Innovation Center of Advanced Microstructures, Nanjing University, Nanjing 210093, China*

[3]*Department of Applied Physics, The Hong Kong Polytechnic University, Hong Kong, China*

Sr_2IrO_4 is predicted to be a candidate for high-temperature superconductivity upon carrier doping, whereas extensive research has proved it challenging to obtain a metallic phase in this compound, especially in thin films. Here, we explore the impact of stoichiometry on the crystallinity, as well as carrier doping and epitaxial strain on the transport properties of $Sr_{2-x}Nd_xIrO_4$ thin films. Via fine tuning the stoichiometry, the crystallinity of Sr_2IrO_4 films can be greatly enhanced, as indicated by the minimized systematic deviations of the x-ray diffraction peak positions. As the cation doping level increases, the resistivity of $Sr_{2-x}Nd_xIrO_4$ films decreases, but it remains semiconducting even at a high level of $x = 0.4$ where the resistivity has dropped by three orders of magnitude. By further applying compressive epitaxial strain, the $Sr_{1.8}Nd_{0.2}IrO_4$ films exhibit a metalliclike behavior with an upturn at low temperature. Our finding reveals a promising combination of electron doping and compressive strain to narrow the band gap and tune the transport properties in iridate films for potential superconductivity.

I. INTRODUCTION

The unconventional superconductivity has been widely researched in transition metal oxides (TMOs), such as $La_{2-x}Ba_xCuO_4$, Sr_2RuO_4, and $Nd_{1-x}Sr_xNiO_2$ [1–3]. However, it seems that no general agreement on the mechanisms of high-temperature superconductors has been reached until now [4]. Thus, it is urgently necessary to seek a new class of high-temperature superconducting (HTSC) materials to provide more insight for the final establishment of HTSC mechanisms. Among Ruddlesden-Popper (RP) iridates $Sr_{n+1}Ir_nO_{3n+1}$, Sr_2IrO_4 ($n = 1$) exhibits the antiferromagnetic $J_{eff} = 1/2$ state on a quasi-two-dimensional square lattice without orbital degeneracy, which is regarded as a $5d$ analog of HTSC cuprates [5–10]. As such, it is theoretically predicted that HTSC materials could be achieved with electron-doping in it [8–10]. To date, electron-doped Sr_2IrO_4 has been revealed to exhibit many cupratelike features, such as Fermi arcs, and a d-wave gap, although the direct signature of superconductivity is still absent [11–14].

For the sake of the possible HTSC phase in iridates, a great amount of effort has been devoted to the synthesis of high-quality single crystals and thin films and the effective carrier doping in this compound. On the one hand, the absence of superconductivity in off-stoichiometry layered ruthenates [2,15–17] and nickelates [3,18,19] films has indicated the negative effects of out-of-phase boundaries (OPBs) in layered superconductors [20]. To exclude these off-stoichiometry defects, it is of great importance to acquire high-quality stoichiometric Sr_2IrO_4 thin films with precise Sr:Ir ratio control. On the other hand, the metallic behavior in electron-doped Sr_2IrO_4 films is still unavailable up to now, despite that its single crystals have shown metallic behaviors [21–24]. The resistivity of Sr_2IrO_4 single crystals can be greatly reduced via La^{3+}, Ce^{4+}, Pr^{3+}, and Sm^{3+} doping, but most of them are still in semiconducting states [22,23,25–27]. Meanwhile, for Sr_2IrO_4 thin films doped by Ce^{4+} under compressive strain, it gives an opposite trend to that in single crystals due to the localization of carriers, in which the effects of electron doping and epitaxial strain cannot be distinguished [20,27–32]. Hence, the growth of high-quality stoichiometric Sr_2IrO_4 thin films should be the prerequisite to realize effective electron doping and study the strain effect for the potential superconductivity in iridates.

In this work, using reactive molecular beam epitaxy (MBE), we report the impact of stoichiometry on crystallinity, as well as electron doping and epitaxial strain on the transport properties of systematically doped $Sr_{2-x}Nd_xIrO_4$ thin films. High-precision crystalline quality control is obtained by minimizing the systematic deviation of the peak positions in x-ray diffraction (XRD). Scanning transmission electron microscopy (STEM) confirms the reliability of our method growing Sr_2IrO_4 thin films. The density functional theory (DFT) calculations are performed for the effect of epitaxial strains on the band structure and density of states (DOSs) of Sr_2IrO_4 thin films. Transport measurements reveal an effective modulation of transport property by a combination of charge carrier doping and compressive strain.

II. EXPERIMENT

The Sr_2IrO_4 thin films were grown epitaxially on (001)-oriented $SrTiO_3$ (STO) and (001)-oriented

*yezhu@polyu.edu.hk
†ynie@nju.edu.cn

(LaAlO$_3$)$_{0.3}$(SrAl$_{0.5}$Ta$_{0.5}$O$_3$)$_{0.7}$ (LSAT) substrates by reactive oxide MBE in a DCA R450 dual growth chamber system. The in-plane pseudocubic lattice constant of Sr$_2$IrO$_4$ is 3.878 Å [33], so that the lattice mismatches of epitaxial Sr$_2$IrO$_4$ films on STO ($a = 3.905$ Å) and LSAT ($a = 3.866$ Å) substrates are $+0.7\%$ and -0.3% respectively, where the tensile (compressive) strain is signed as $+ (-)$. The TiO$_2$-terminated step-and-terrace surface of STO substrate was obtained by the standard etching technique as reported previously [34]. For the Sr$_2$IrO$_4$ grown on LSAT substrates, a 10-u.c.-thick STO buffer layer with a TiO$_2$-terminated surface was prepared before the growth in order to exclude the impact of exact interface configurations. The films were grown under an oxidant (distilled O$_3$) background pressure of 2×10^{-6} Torr and at a substrate temperature of 800 °C. Besides, all these films were grown by a codeposition method that deposits all elements with a proper flux ratio simultaneously. The growth process was monitored by *in situ* reflection high-energy electron diffraction (RHEED), with glancing electron beam parallel to either the [110]$_p$ or the [100]$_p$ directions, where the subscript p denotes pseudocubic indices. The crystallinity of the films was characterized by XRD (Bruker D8 Discover). Cross-sectional STEM samples were prepared using a Thermo Fisher Helios 5CX dual-beam FIB/SEM (focused ion beam/scanning electron microscope). Atomic-resolution annular dark-field (ADF) STEM imaging was conducted with a double Cs corrected Spectra 300 (TFS, USA) operated at the accelerating voltage of 300 kV and equipped with a Super-X energy-dispersive x-ray spectroscopy (EDS) spectrometer. Temperature-dependent resistivity was measured via the standard van der Pauw geometry using the ultrasonic aluminum wire bonding method in a homemade transport properties measurement system.

III. RESULTS AND DISCUSSION

A. XRD analysis of cation stoichiometry on Sr$_2$IrO$_4$ thin films

The precise control of high quality Sr$_2$IrO$_4$ thin film growth has been shown to be challenging. By using the same SrIrO$_3$ target in the pulse laser deposition (PLD) growth, a slight variation of the growth conditions can result in strikingly different phases, including SrIrO$_3$, Sr$_2$IrO$_4$, Sr$_3$Ir$_2$O$_7$, and a mixture of these phases [35,36]. These results imply the volatility of the IrO$_x$ and the great challenges in synthesizing high quality iridate films with precise stoichiometry. As the flux of all sources can be controlled independently in MBE, we can investigate the effects of the Sr:Ir flux ratio on the crystallinity of Sr$_2$IrO$_4$ thin films.

All these Sr$_2$Ir$_{1+y}$O$_4$ thin films hold clear RHEED patterns without any impurity phase diffraction, as shown in Fig. S2 of the Supplemental Material [37], even when Ir flux is changed by 30%. Also, the XRD 2θ-ω scans along the [00L] direction exhibit a reasonably good pattern, showing sharp (00L) reflections with clear Kiessig fringes for a wide range. The lack of sensitivity of RHEED and XRD characterizations to the sample variations explains the difficulty in obtaining Sr$_2$IrO$_4$ films with ideal crystal quality. Interestingly, by careful
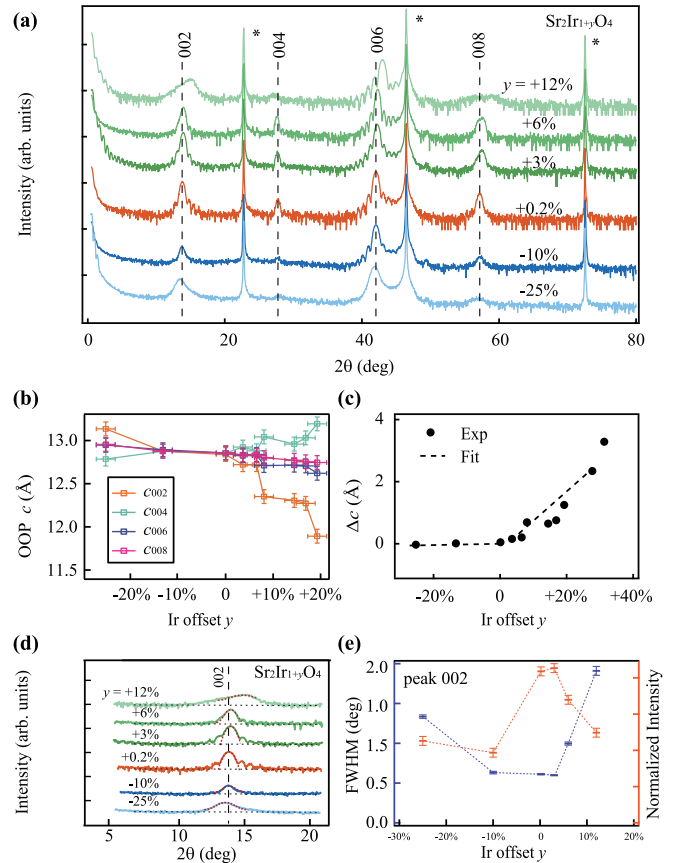

FIG. 1. (a) XRD 2θ-ω scans of 10-u.c.-thick Sr$_2$Ir$_{1+y}$O$_4$ thin films on STO (001) with various Ir concentrations. Diffraction peaks of STO are identified by asterisks. The black dashed lines are guides for the optimal peak positions. (b) Out-of-plane (OOP) lattice constant c from (002), (004), (006), and (008) versus Ir flux offset y, respectively. The vertical (horizontal) error bars represent the variance coming from measurement errors of lattice constants (Ir flux ratio). (c) The values of Δc ($c_{004} - c_{002}$) versus Ir flux offset y using Eq. (1). Black dashed lines are the linear fitting results. (d) Extended XRD 2θ-ω scans of 002 peaks in Sr$_2$Ir$_{1+y}$O$_4$ thin films. (e) FWHM (full width at half maximum) and normalized intensity of 002 peaks.

analysis of the XRD data, the peak positions in XRD actually exhibit slight systematic dependence on the stoichiometry in Fig. 1(a). For a perfect crystal, all the (00l) reflections are from the same set of parallel planes and the calculated c lattice constants should be the same. The difference in Δc reflects the imperfection of the crystalline quality, which can help to calibrate the Sr:Ir flux ratio finely beyond the quartz-crystal microbalance (QCM) calibration. We observe a reverse trend of lattice constant c from (002) and (004) as the Ir flux is changed correspondingly. We use the (00l) indexes of Sr$_2$IrO$_4$ to calculate the c lattice constants and Δc ($c_{004} - c_{002}$) increases as Ir dosage is changed:

$$\Delta c = c_{004} - c_{002}. \quad (1)$$

An explanation of the appearance of Δc is related to the appearance of Sr$_3$Ir$_2$O$_7$ phase when Ir is rich. We show that a substantial increase of Ir concentration will eventually result in a Sr$_3$Ir$_2$O$_7$ phase, which is shown in Fig. S3 of the Supplemental Material [37]. Since Sr$_2$IrO$_4$ is the $n = 1$
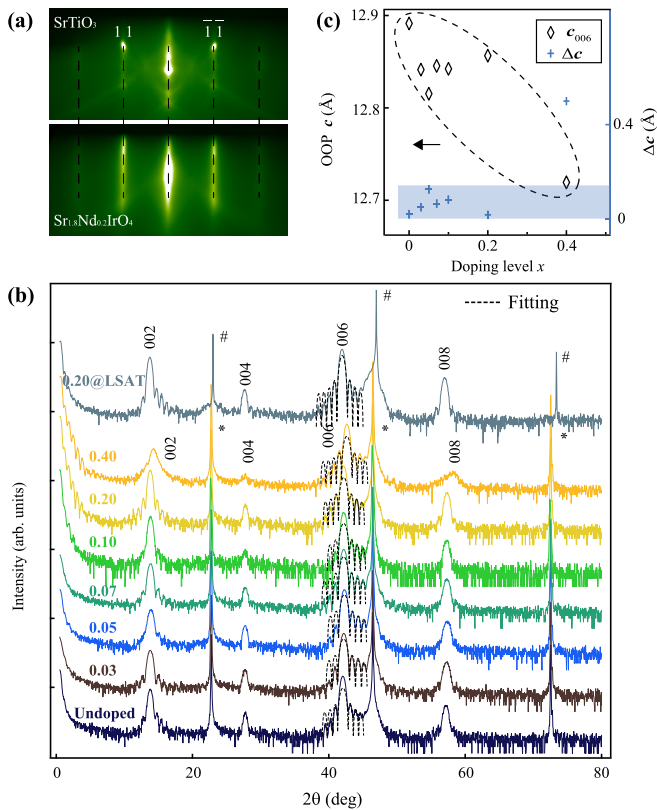
FIG. 2. (a) RHEED patterns of the STO substrate and the $Sr_{1.8}Nd_{0.2}IrO_4$ thin film, along $[110]_p$ azimuth, indicated as black dashed lines. (b) XRD 2θ-ω scans of 10-u.c.-thick $Sr_{2-x}Nd_xIrO_4$ thin films on STO (001) ($x = 0\%$, 3%, 5%, 7%, 10%, 20%, 40%) and on LSAT (001) ($x = 20\%$) substrates. Diffraction peaks of STO and LSAT substrates are identified by asterisks and sharps, respectively. The Kiessig fringes are fitted as the black dashed lines. (c) OOP lattice constants, c (left axis), and values of Δc (right axis) of $Sr_{2-x}Nd_xIrO_4$ on STO substrate as a function of doping level x. The c values, extracted from (006) peaks, are denoted by black diamonds. The deviations of two kinds of c values, from (002) and (004), are recorded by Δc at the right axis, denoted by blue crosses.

end member of the Ruddlesden-Popper series $[Sr_{n+1}Ir_nO_{3n+1}$, $(SrIrO_3)_n(SrO)]$, there is no well-ordered crystalline structure made of SrO and IrO_2 building blocks when the dosage ratio Sr:Ir is higher than 2:1. The excess Sr may form some SrO impurities that does not appear on the XRD scans. As a result, the crossing point between the incline line and the horizontal line is the ideal Sr_2IrO_4 structure with ideal 2:1 stoichiometry, shown in Fig. 1(c), as the intensity, area, and width of the diffraction peaks are closely related to the volume and ordering of the crystalline structure. In Figs. 2(d) and 2(e), the intensity, area, and full width at half maximum (FWHM) of the (002) diffraction peaks clearly reach a maximum or minimum at the optimal dosage, which can be utilized to optimize the growth of iridate films. Additionally, the absolute value of Δc reflects the deviation of the practical ratio Sr:Ir away from the ideal case, as $\Delta c = 0$. In other words, we take XRD to measure the slight structural aberration caused by off-stoichiometry, and it feeds back on the growth with an uncertainty of 0.8% in Ir flux ratio corresponding to

$\Delta c < 0.1$ Å. The puny shifts in multiple diffraction positions can be collected for structural characterization associated with STEM. As the amount of Ir flux is reduced (increased), the value of Δc is negative (positive), which is attributed to the insufficient (excess) IrO_2, corresponding to two types of OPBs to maintain the Ir vacancies (the excess IrO_x layers). These two types of OPBs were observed in the STEM images previously in $n = 1$ RP films, such as Sr_2RuO_4 and Sr_2TiO_4 [17,38,39] corresponding to the minute deviation in the cation stoichiometry. This practical method for Sr_2IrO_4 film synthesis can help to calibrate the cation stoichiometry in Sr_2IrO_4 growth precisely. The resistivity of these off-stoichiometry $Sr_2Ir_{1+y}O_4$ thin films on STO (001) is shown in Fig. S4 [37] which is different from the Sr_2IrO_4 film. The excess/deficient Ir seems to result in a lower/higher resistivity, which may be caused by the formation of different types of faults. Nonetheless, all these imperfect samples show large increase of the resistivity due to the enhance defect scattering at low temperature.

B. Structural characterizations on $Sr_{2-x}Nd_xIrO_4$ thin films

Since we can optimize the stoichiometry in Sr_2IrO_4 thin films based on the values of Δc, it is possible to realize precise ion substitution for electron doping. These $Sr_{2-x}Nd_xIrO_4$ ($x = 0\%$, 3%, 5%, 7%, 10%, 20%, and 40%) films are grown by a codeposition method, which is discussed in the Supplemental Material and illustrated in Fig. S1 [37]. The thickness of films can be estimated by fitting the specific thickness fringes in Fig. 2(b) as 10 u.c. approximately, which is in good correspondence with the nominal thickness controlled by the deposition time. In addition, the Kiessig fringes indicate smooth film surface and sharp interface in these films. Moreover, the out-of-plane (OOP) lattice constant of $Sr_{2-x}Nd_xIrO_4$ film on LSAT is larger than that on STO, in line with the in-plane compressive strain imposed by LSAT.

As Fig. 2(c) shows, the quality of all doped films is examined on the basis of Δc, whose offset of Ir flux is less than 1% as estimated by Fig. 1(d), except for $x = 40\%$, probably caused by lattice distortion from heavy doping. Here, the $x = 20\%$ sample on LSAT is motivated because 20% electron doping is at the center of the predicted superconducting dome [8–10]. The Δc of $Sr_{1.8}Nd_{0.2}IrO_4$ thin film on LSAT is smaller than 0.02 Å, corresponding to the Ir flux offset of less than 0.2%. Also, our films are more stable in air compared to surface-potassium-doped Sr_2IrO_4, confirmed by *ex situ* characterizations [11,14,22,40].

Reciprocal space mappings (RSMs) indicate these $Sr_{2-x}Nd_xIrO_4$ films are fully constrained to the substrates, as shown in Fig. 3(a). Furthermore, the (10$\underline{1}$1) patterns are also clearly observed, which are typically too faint to identify for the off-stoichiometry films. In Fig. 3(b), the cross-sectional ADF-STEM image of the $Sr_{1.8}Nd_{0.2}IrO_4$ film reveals the layered structure consisting of alternatively stacked perovskite and rocksalt units. Meanwhile, a sharp interface without obvious cation interdiffusion can be ascertained through the corresponding EDS maps in Fig. 3(c). In particular, there is no chemical segregation in $Sr_{2-x}Nd_xIrO_4$ thin films, suggesting uniform doping. The Nd concentrations from EDS results are
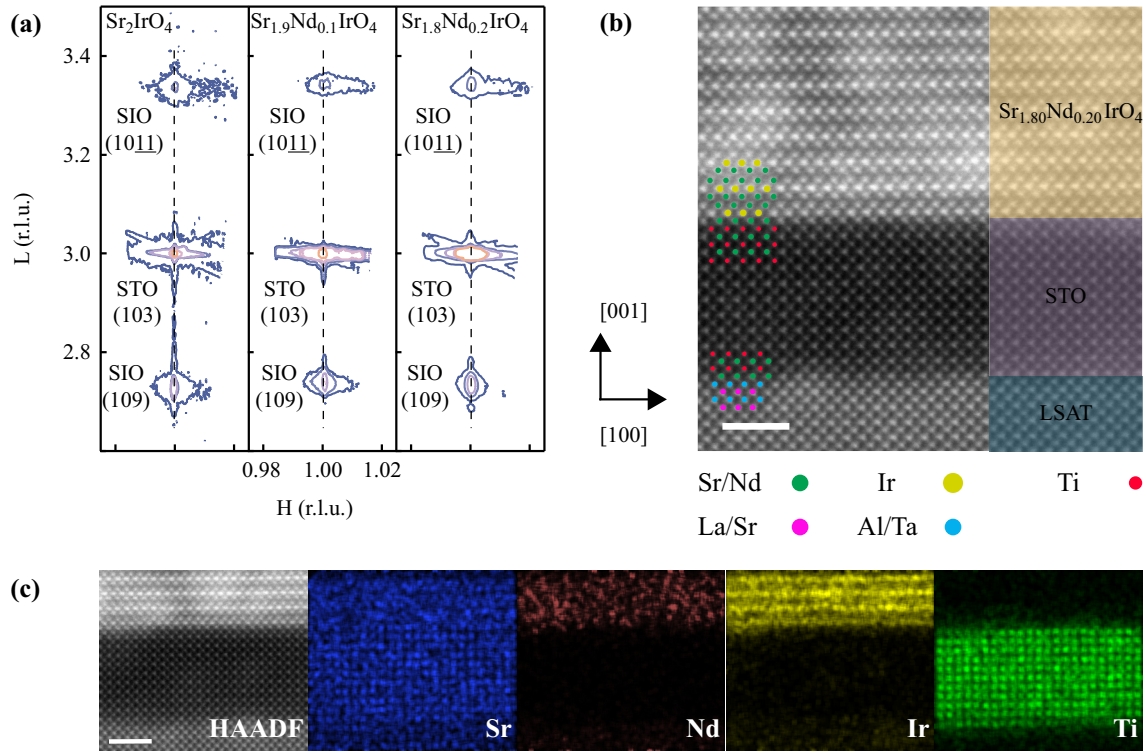
FIG. 3. (a) RSMs of the 10-u.c.-thick $Sr_{2-x}Nd_xIrO_4$ thin films, with $x = 0\%$, 10%, and 20% around STO (103) diffraction peak. The black dashed lines indicate the films are fully strained to the STO substrates. (b) Cross-sectional ADF-STEM image of the $Sr_{0.8}Nd_{0.2}IrO_4$ thin film with a 10-u.c.-thick STO buffer layer on LSAT, with the crystal structure model overlaid. Scale bar, 2 nm. (c) Enlarged view of the ADF-STEM image shown in (b), and the corresponding EDS maps near the interface, for Sr, Nd, Ir, and Ti. Scale bar, 2 nm.

consistent with the nominal doping levels as shown in Table S1 [37].

C. Transport properties in $Sr_{2-x}Nd_xIrO_4$ thin films

The temperature-dependent resistivity of $Sr_{2-x}Nd_xIrO_4$ thin films was measured by the van der Pauw method, as shown in Fig. 4(a). The $Sr_{2-x}Nd_xIrO_4$ ($x = 0\%$, 3%, 5%, 7%, 10%, 20%, and 40%) films on STO exhibit semiconducting behaviors, as shown in Fig. 4(a). The replacement of Nd^{3+} on the Sr site is expected to introduce more carriers, thus the resistivity of Nd-doped films falls significantly. In particular, the resistivity drops by at least two orders of magnitude when $x = 20\%$. It is well established that the $\rho \sim T$ curves can be well fitted according to the Arrhenius-type behavior in the high temperature range [22,41]. The resistivity data between 150 and 250 K were taken to estimate the evolution of energy gap, which could be determined from $\ln \rho \sim T^{-1}$ curves, and the results are summarized in Fig. 4(c). The activation energy for the Nd-doped samples on STO decreasees from 88 meV for $x = 0$ to 3.8 meV for $x = 40\%$. It seems that the decrease of the activation energy meets a saturation when $x = 20\%$, at which the sample is still semiconducting. It is worth noting that the resistivity decreases further as the doping level increases, to $x = 40\%$, though its crystalline quality is relatively poor as indicated by Δc in Fig. 2(c).

Considering the crystalline quality degeneration caused by heavy doping at $x = 40\%$, we focus our study of the films with $x = 20\%$, which is actually the optimal doping level in the predicted superconducting dome [8–10]. In order to

further narrow the band gap, we apply the compressive epitaxial strain on these doped samples. To understand the strain effects on the transport behaviors in Sr_2IrO_4 films, the electron band structures and DOS of free-standing and strained Sr_2IrO_4 are calculated by the DFT in the generalized gradient approximation implemented in the Vienna *ab initio* simulation package (VASP) code [42,43], in which the projected augmented wave method [44,45] and the Perdew-Burke-Ernzerhof revised for solids exchange-correlation [46] are used (see Supplemental Material for more details [37]). The compressive strain can narrow the band gap in Sr_2IrO_4, as shown in Fig. 5 and Fig. S5 of the Supplemental Material. The total DOS of Sr_2IrO_4 films indicates a clear energy gap near the Fermi energy for the free-standing condition. The band gap gradually shrinks as the in-plane strain increases. This tendency is in accordance with transport experimental results that the conductivity of Sr_2IrO_4 films increases with increasing in-plane compressive strain. However, experimental reports show that undoped Sr_2IrO_4 films grown on LSAT substrates with a pure compressive strain up to -0.3% remain insulating [31].

In contrast, our experiments show that the $Sr_{1.8}Nd_{0.2}IrO_4$ films with compressive strain imposed by LSAT demonstrate a lower resistivity in the whole temperature range, and the metalliclike behavior is observed. By a combination of electron doping and compressive strain modulation, a low-temperature metal-insulator transition ($T_{MIT} \sim 45$ K) is finally observed in $Sr_{1.8}Nd_{0.2}IrO_4$ films on LSAT as enlarged in Fig. 4(b). The effect of the biaxial compressive strain is proved to be helpful for the metallic behavior in $Sr_{2-x}Nd_xIrO_4$
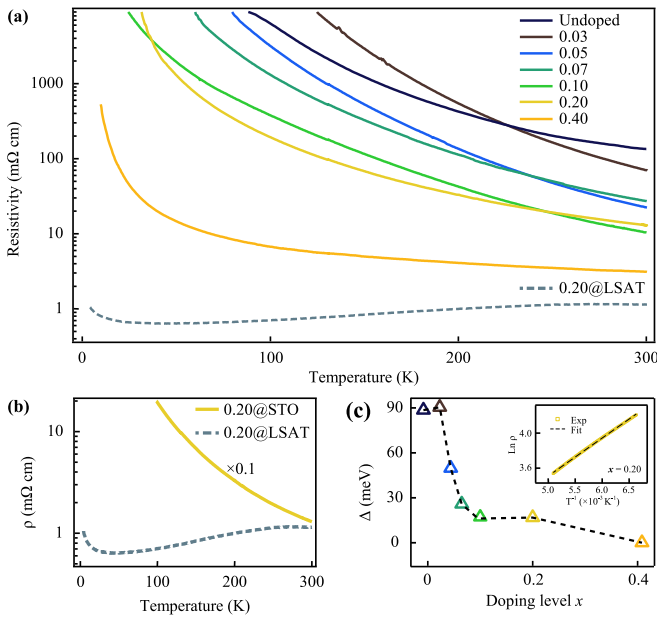
FIG. 4. (a) Temperature-dependent resistivity of 10-u.c.-thick $Sr_{2-x}Nd_xIrO_4$ thin films for $x = 0\%$, 3%, 5%, 7%, 10%, 20%, and 40% on STO by solid lines, and for $x = 20\%$ on LSAT marked as a dashed line. (b) Enlarged image for resistivity of $Sr_{1.8}Nd_{0.2}IrO_4$ on STO and LSAT. The resistivity of $Sr_{1.8}Nd_{0.2}IrO_4$ on STO is rescaled for clarity. (c) The activation energy Δ of $Sr_{2-x}Nd_xIrO_4$ thin films on STO, as a function of doping levels x, which are calculated by the thermal activation model in the range 150–250 K. The black dashed line is a guide for the eyes. Inset: logarithmic resistivity of $x = 20\%$ on STO as a function of T^{-1} fit with straight lines to indicate the thermal activation model.

films, which can be explained by the enhancement on the hopping integral and the diminishment on the strength of electronic correlation [32,47]. The conductivity of partially relaxed $Sr_{1.8}Nd_{0.2}IrO_4$ film on $LaAlO_3$ substrates is weakened, due to the strain-induced disorders from the high misfit [29,31], as shown in Fig. S6.

IV. CONCLUSIONS

In conclusion, the effects of electron doping and epitaxial compressive strain in $Sr_{2-x}Nd_xIrO_4$ ($x = 0 - 40\%$) thin films have been demonstrated. A quantitative analysis of the XRD peak position shifts has been determined to be an effective route to precisely control the sample quality of $Sr_{2-x}Nd_xIrO_4$ films via optimizing the stoichiometry. Measurements of the transport properties in doped samples show that, as the doping level increases, the resistivity of $Sr_{2-x}Nd_xIrO_4$ films reduces, and the activation energy decreases correspondingly. The results from the DFT calculations confirm the modulation of epitaxial compressive strains on the Sr_2IrO_4 films to narrow the band gap. By further applying the compressive strain,
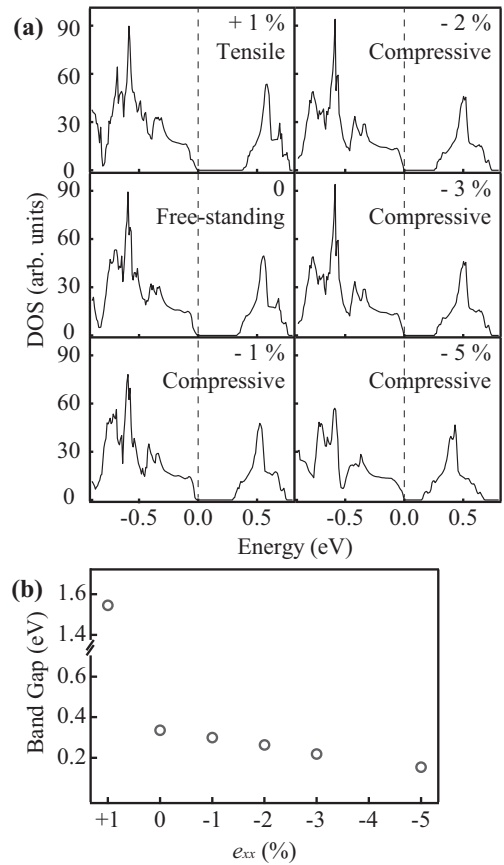

FIG. 5. (a) DFT band structures of Sr_2IrO_4 with different strain states indicated in corresponding panels. The dashed lines refer to the Fermi energy. (b) Variation of the band gaps with strain e_{xx}. The values of band gaps are extracted from the total DOSs under various in-plane strain states.

$Sr_{1.8}Nd_{0.2}IrO_4$ films exhibit a metallic behavior with an upturn at low temperature. Our work thus demonstrates the effective tuning of the band gap and transport properties of Sr_2IrO_4 thin films by a combination of carrier doping and compressive strain, paving the way for future exploration of HTSC in the Sr_2IrO_4 thin film.

[1] J. G. Bednorz and K. A. Muller, Possible high-T_c superconductivity in the Ba-La-Cu-O system, Z. Phys. B: Condens. Matter **64**, 189 (1986).

[2] Y. Maeno, H. Hashimoto, K. Yoshida, S. Nishizaki, T. Fujita, J. G. Bednorz, and F. Lichtenberg, Exploiting dimensionality and defect mitigation to create tunable

microwave dielectrics, Nature (London) **372**, 532 (1994).

[3] D. F. Li, K. Lee, B. Y. Wang, M. Osada, S. Crossley, H. R. Lee, Y. Cui, Y. Hikita, and H. Y. Hwang, Superconductivity in an infinite-layer nickelate, Nature (London) **572**, 624 (2019).

[4] B. Keimer, S. A. Kivelson, M. R. Norman, S. Uchida, and J. Zaanen, From quantum matter to high-temperature superconductivity in copper oxides, Nature (London) **518**, 179 (2015).

[5] B. J. Kim, H. Jin, S. J. Moon, J. Y. Kim, B. G. Park, C. S. Leem, J. Yu, T. W. Noh, C. Kim, S. J. Oh, J. H. Park, V. Durairaj, G. Cao, and E. Rotenberg, Novel $J_{eff} = 1/2$ Mott State Induced by Relativistic Spin-Orbit Coupling in Sr_2IrO_4, Phys. Rev. Lett. **101**, 076402 (2008).

[6] B. J. Kim, H. Ohsumi, T. Komesu, S. Sakai, T. Morita, H. Takagi, and T. Arima, Phase-Sensitive Observation of a Spin-Orbital Mott State in Sr_2IrO_4, Science **323**, 1329 (2009).

[7] G. Jackeli and G. Khaliullin, Mott Insulators in the Strong Spin-Orbit Coupling Limit: From Heisenberg to a Quantum Compass and Kitaev Models, Phys. Rev. Lett. **102**, 017205 (2009).

[8] Z. Y. Meng, Y. B. Kim, and H. Y. Kee, Odd-Parity Triplet Superconducting Phase in Multiorbital Materials with a Strong Spin-Orbit Coupling: Application to Doped Sr_2IrO_4, Phys. Rev. Lett. **113**, 177003 (2014).

[9] F. Wang and T. Senthil, Twisted Hubbard Model for Sr_2IrO_4: Magnetism and Possible High Temperature Superconductivity, Phys. Rev. Lett. **106**, 136402 (2011).

[10] H. Watanabe, T. Shirakawa, and S. Yunoki, Monte Carlo Study of an Unconventional Superconducting Phase in Iridium Oxide $J_{eff} = 1/2$ Mott Insulators Induced by Carrier Doping, Phys. Rev. Lett. **110**, 027002 (2013).

[11] Y. K. Kim, O. Krupin, J. D. Denlinger, A. Bostwick, E. Rotenberg, Q. Zhao, J. F. Mitchell, J. W. Allen, and B. J. Kim, Fermi arcs in a doped pseudospin-1/2 Heisenberg antiferromagnet, Science **345**, 187 (2014).

[12] A. de la Torre, S. McKeown Walker, F. Y. Bruno, S. Ricco, Z. Wang, I. Gutierrez Lezama, G. Scheerer, G. Giriat, D. Jaccard, C. Berthod, T. K. Kim, M. Hoesch, E. C. Hunter, R. S. Perry, A. Tamai, and F. Baumberger, Collapse of the Mott Gap and Emergence of a Nodal Liquid in Lightly Doped Sr_2IrO_4, Phys. Rev. Lett. **115**, 176402 (2015).

[13] Y. J. Yan, M. Q. Ren, H. C. Xu, B. P. Xie, R. Tao, H. Y. Choi, N. Lee, Y. J. Choi, T. Zhang, and D. L. Feng, Electron-Doped Sr_2IrO_4: An Analogue of Hole-Doped Cuprate Superconductors Demonstrated by Scanning Tunneling Microscopy, Phys. Rev. X **5**, 041018 (2015).

[14] Y. K. Kim, N. H. Sung, J. D. Denlinger, and B. J. Kim, Observation of a d-wave gap in electron-doped Sr_2IrO_4, Nat. Phys. **12**, 37 (2016).

[15] Z. Q. Mao, Y. Mori, and Y. Maeno, Suppression of superconductivity in Sr_2RuO_4 caused by defects, Phys. Rev. B **60**, 610 (1999).

[16] M. A. Zurbuchen, Y. F. Jia, S. Knapp, A. H. Carim, D. G. Schlom, L. N. Zou, and Y. Liu, Suppression of superconductivity by crystallographic defects in epitaxial Sr_2RuO_4 films, Appl. Phys. Lett. **78**, 2351 (2001).

[17] G. Kim, Y. E. Suyolcu, J. Herrero-Martin, D. Putzky, H. P. Nair, J. P. Ruf, N. J. Schreiber, C. Dietl, G. Christiani, G. Logvenov, M. Minola, P. A. van Aken, K. M. Shen, D. G. Schlom, and B. Keimer, Electronic and vibrational signatures of ruthenium

vacancies in Sr_2RuO_4 thin films, Phys. Rev. Mater. **3**, 094802 (2019).

[18] Y. Li, W. Sun, J. Yang, X. Cai, W. Guo, Z. Gu, Y. Zhu, and Y. Nie, Impact of Cation Stoichiometry on the Crystalline Structure and Superconductivity in Nickelates, Front. Phys. **9**, 719534 (2021).

[19] Q. Li, C. He, J. Si, X. Zhu, Y. Zhang, and H.-H. Wen, Absence of superconductivity in bulk $Nd_{1-x}Sr_xNiO_2$, Mater. Commun. **1**, 16 (2020).

[20] M. A. Zurbuchen, W. Tian, X. Q. Pan, D. Fong, S. K. Streiffer, M. E. Hawley, J. Lettieri, Y. Jia, G. Asayama, S. J. Fulk, D. J. Comstock, S. Knapp, A. H. Carim, and D. G. Schlom, Morphology, structure, and nucleation of out-of-phase boundaries (OPBs) in epitaxial films of layered oxides, J. Mater. Res. **22**, 1439 (2007).

[21] O. B. Korneta, T. Qi, S. Chikara, S. Parkin, L. E. De Long, P. Schlottmann, and G. Cao, Electron-doped $Sr_2IrO_{4-\delta}$ $(0 \leqslant \delta \leqslant 0.04)$: Evolution of a disordered $J_{eff} = 1/2$ Mott insulator into an exotic metallic state, Phys. Rev. B **82**, 115117 (2010).

[22] M. Ge, T. F. Qi, O. B. Korneta, D. E. De Long, P. Schlottmann, W. P. Crummett, and G. Cao, Lattice-driven magnetoresistivity and metal-insulator transition in single-layered iridates, Phys. Rev. B **84**, 100402(R) (2011).

[23] H. Huang, P. Ji, Y. Xie, H. Han, and B. Ge, Exploration of the bond angle and charge carrier density by rare-earth doping in Sr_2IrO_4, Phys. Rev. Mater. **4**, 115001 (2020).

[24] B. Hu, H. Zhao, Y. Zhang, P. Schlottmann, F. Ye, and G. Cao, Correlation between antiferromagnetic and Mott states in spin orbit coupled Sr_2IrO_4: A study of $Sr_2Ir_{1-x}M_xO_4$ (M = Fe or Co), Phys. Rev. B **103**, 115122 (2021).

[25] H. Liu, D. Liang, J. Bian, Y. Feng, Y. Xie, and B. Fang, Suppressed antiferromagnetic ordering and enhanced electrical conduction in doped iridate $Sr_{2-x}Pr_xIrO_4$, Mater. Res. Express. **7**, 026102 (2020).

[26] C. Zhu, S. Liu, J. Cheng, B. Li, P. Dong, and Z. Wang, Non-monotonic effect of the electronic transport and magnetic properties in a Sm-doped $Sr_{2-x}Sm_xIrO_4$ system, Europhys. Lett. **124**, 17004 (2018).

[27] M. Ito, M. Uchida, Y. Kozuka, K. S. Takahashi, and M. Kawasaki, Effective carrier doping and metallization in $La_xSr_{2-x-y}Ba_yIrO_{4-\delta}$ thin films, Phys. Rev. B **93**, 045139 (2016).

[28] Y.-S. Zhang, Y.-Q. Hu, Y. Cai, X. Deng, Z. Guan, N. Zhong, P.-H. Xiang, and C.-G. Duan, Effect of Ce doping on the structural, transport and magnetic properties of Sr_2IrO_4 epitaxial films, J. Phys. D **54**, 405304 (2021).

[29] J. Nichols, J. Terzic, E. G. Bittle, O. B. Korneta, L. E. De Long, J. W. Brill, G. Cao, and S. S. A. Seo, Tuning electronic structure via epitaxial strain in Sr_2IrO_4 thin films, Appl. Phys. Lett. **102**, 141908 (2013).

[30] B. Kim, B. H. Kim, K. Kim, and B. I. Min, Substrate-tuning of correlated spin-orbit oxides revealed by optical conductivity calculations, Sci. Rep. **6**, 27095 (2016).

[31] M. Souri, J. G. Connell, J. Nichols, J. Terzic, G. Cao, and A. Seo, Crossover between Mott and Efros-Shklovskii variable-range hopping in Sr_2IrO_4 epitaxial thin films by misfit strain and isovalent doping, J. Appl. Phys. **126**, 185101 (2019).

[32] E. Paris, Y. Tseng, E. M. Parschke, W. Zhang, M. H. Upton, A. Efimenko, K. Rolfs, D. E. McNally, L. Maurel, M. Naamneh, M. Caputo, V. N. Strocov, Z. Wang, D. Casa, C. W. Schneider,

E. Pomjakushina, K. Wohlfeld, M. Radovic, and T. Schmitt, Strain engineering of the charge and spin-orbital interactions in Sr_2IrO_4, Proc. Natl. Acad. Sci. USA **117**, 24764 (2020).

[33] G. Cao and P. Schlottmann, The challenge of spin-orbit-tuned ground states in iridates: A key issues review, Rep. Prog. Phys. **81**, 042502 (2018).

[34] M. Kawasaki, K. Takahashi, T. Maeda, R. Tsuchiya, M. Shinohara, O. Ishiyama, T. Yonezawa, M. Yoshimoto, and H. Koinuma, Atomic control of the $SrTiO_3$ crystal surface, Science **266**, 1540 (1994).

[35] H. Xu, Z. Cui, X. Zhai, and Y. Lu, Growth of high quality Sr_2IrO_4 epitaxial thin films on conductive substrates, Chin. Phys. B **28**, 78102 (2019).

[36] J. Yang, L. Hao, P. Nanney, K. Noordhoek, D. Meyers, L. Horak, J. Sanchez, J.-H. Chu, C. Nelson, M. P. M. Dean, and J. Liu, Epitaxial stabilization of $Sr_3Ir_2O_7$ thin films, Appl. Phys. Lett. **114**, 182401 (2019).

[37] See Supplemental Material at http://link.aps.org/supplemental/10.1103/PhysRevB.107.235152 for method and details of DFT calculation.

[38] M. A. Zurbuchen, Y. F. Jia, S. Knapp, A. H. Carim, D. G. Schlom, and X. Q. Pan, Defect generation by preferred nucleation in epitaxial $Sr_2RuO_4/LaAlO_3$, Appl. Phys. Lett. **83**, 3891 (2003).

[39] M. R. Barone, N. M. Dawley, H. P. Nair, B. H. Goodge, M. E. Holtz, A. Soukiassian, E. E. Fleck, K. Lee, Y. Jia, T. Heeg, R. Gatt, Y. Nie, D. A. Muller, L. F. Kourkoutis, and D. G. Schlom, Improved control of atomic layering in perovskite-related homologous series, APL Mater. **9**, 021118 (2021).

[40] S. Peng, C. Lane, Y. Hu, M. Guo, X. Chen, Z. Sun, M. Hashimoto, D. Lu, Z.-X. Shen, T. Wu, X. Chen, R. S. Markiewicz, Y. Wang, A. Bansil, S. D. Wilson, and J. He, Electronic nature of the pseudogap in electron-doped Sr_2IrO_4, npj Quantum Mater. **7**, 58 (2022).

[41] C. Lu, A. Quindeau, H. Deniz, D. Preziosi, D. Hesse, and M. Alexe, Crossover of conduction mechanism in Sr_2IrO_4 epitaxial thin films, Appl. Phys. Lett. **105**, 082407 (2014).

[42] G. Kresse and J. Furthmuller, Efficiency of *ab-initio* total energy calculations for metals and semiconductors using a plane-wave basis set, Comput. Mater. Sci. **6**, 15 (1996).

[43] G. Kresse and J. Furthmuller, Efficient iterative schemes for *ab initio* total-energy calculations using a plane-wave basis set, Phys. Rev. B **54**, 11169 (1996).

[44] P. E. Blochl, Projector augmented-wave method, Phys. Rev. B **50**, 17953 (1994).

[45] G. Kresse and D. Joubert, From ultrasoft pseudopotentials to the projector augmented-wave method, Phys. Rev. B **59**, 1758 (1999).

[46] J. P. Perdew, A. Ruzsinszky, G. I. Csonka, O. A. Vydrov, G. E. Scuseria, L. A. Constantin, X. L. Zhou, and K. Burke, Restoring the Density-Gradient Expansion for Exchange in Solids and Surfaces, Phys. Rev. Lett. **100**, 136406 (2008).

[47] S. Lee, Y.-S. Seo, E. Jung, S. Roh, M. Lee, H. Y. Choi, J. H. Kim, N. Lee, Y. J. Choi, and J. Hwang, Evolution of the electronic structure of Ru-doped single-crystal iridates $Sr_2Ir_{1-x}Ru_xO_4$, Phys. Rev. B **104**, 165106 (2021).